Experimental Determination of the Shear Rate in a Stirred Tank with a Non-Newtonian Fluid: Carbopol

J.-C. Gabelle
Université de Toulouse, INSA, LISBP, 135 Avenue de Rangueil, F-31077 Toulouse, France

INRA UMR792 Ingénierie des Systèmes Biologiques et des Procédés, Toulouse, France

CNRS, UMR5504, F-31400 Toulouse, France

ADEME French Environment and Energy Management Agency 20, avenue du Grésillé-BP 90406 49004 Angers Cedex 01 France

IFP Energies nouvelles, Rond-point de l'échangeur de Solaize, BP3, 69360 Solaize, France

J. Morchain
Université de Toulouse, INSA, LISBP, 135 Avenue de Rangueil, F-31077 Toulouse, France

INRA UMR792 Ingénierie des Systèmes Biologiques et des Procédés, Toulouse, France

CNRS, UMR5504, F-31400 Toulouse, France

D. Anne-Archard
Université de Toulouse, INPT, UPS, IMFT, Allée C. Soula, F-31400 Toulouse, France

F. Augier
IFP Energies nouvelles, Rond-point de l'échangeur de Solaize, BP3, 69360 Solaize, France

A. Liné
Université de Toulouse, INSA, LISBP, 135 Avenue de Rangueil, F-31077 Toulouse, France

INRA UMR792 Ingénierie des Systèmes Biologiques et des Procédés, Toulouse, France

CNRS, UMR5504, F-31400 Toulouse, France

DOI 10.1002/aic.13973
Published online December 20, 2012 in Wiley Online Library (wileyonlinelibrary.com).

The local shear rate generated in a cylindrical tank equipped with a Rushton turbine was investigated using particle image velocimetry in a shear-thinning fluid (Carbopol). This non-Newtonian fluid was used in an attempt to mimic fermentation broths. Three Reynolds numbers corresponding to the transition regime were investigated. The hydrodynamics is analyzed, and the velocity field is decomposed by proper orthogonal decomposition into mean flow, organized motion, and turbulence. Then, the contributions of each flow structure to the total dissipation of kinetic energy are presented. The spatial heterogeneity of shear rate is discussed and a new expression is proposed for shear rate. This work shows that the local shear rate is highly heterogeneous in a tank. Future works will need to focus on other types of stirrer and investigate the effect of scaling up reactors on the shear rate heterogeneity. © 2012 American Institute of Chemical Engineers *AIChE J,* 59: 2251–2266, 2013

Keywords: non-Newtonian fluid, proper orthogonal decomposition, mixing, particle image velocimetry, stirred tank, shear rate, dissipation

Introduction

In the biochemical industry, stirred tanks are commonly used for fermentation processes as they give good mixing and mass-transfer capacities. Over the years, numerous studies have been performed on the topic in the aim of understanding and quantifying the physical phenomena occurring in this type of reactor. Because of the difficulties of studying complex flow, most of the previous works were done in Newtonian or laminar non-Newtonian fluids. In contrast, biological broths (e.g., filamentous cultivation), are hardly ever Newtonian and, because of the scale, bioreactors are run in the turbulent or locally transitional regime.

During the fermentation process, the rheology of the medium evolves from viscous to highly non-Newtonian

Correspondence concerning this article should be addressed to A. Liné at alain.line@insa-toulouse.fr.

© 2012 American Institute of Chemical Engineers

behavior. The increase of apparent viscosity of the fluid tends to decrease mass-transfer performance.[1] Consequently, to maintain the oxygen level in the reactor, aeration and agitation have to be increased. This leads to an increase of the shear rate that can cause shear damage to microorganisms.[2] It has been proved that the morphology and the productivity of filamentous cultures are affected by hydrodynamic conditions. Many articles have focused on this topic[3–6] with both *in situ* or *ex situ* experiments. Morphological or productivity results are often correlated with global parameters such as impeller speed, power draw, volume around the impeller, and so forth. Actually, the most important parameter, which is difficult to access in biological media, is the local shear rate.

Some correlations exist in the literature to estimate the average shear rate in the reactor. The classic Metzner–Otto[7] correlation shows that the average shear rate is proportional to the impeller speed N.

$$\dot{\gamma}_{MO} = k_S N. \tag{1}$$

The proportionality constant depends on the type of impeller ($k_S = 11.5$ for a Rushton turbine). Calderbank and Moo-Young[8] modified this constant with rheological parameters (K and n from a power law model). These two approaches have been validated in laminar experiments but also seem to be widely used in turbulent regime. Kelly and Gigas[9] used computational fluid dynamics (CFD) to determine the average shear rate in the transitional regime with an axial flow impeller. They found that the Metzner–Otto correlation resulted in an under prediction of the average shear rate. They proposed a modified proportionality constant that fitted their predicted data ($k_S = 33.3$). Sanchez Perez et al.[10] used the data of Kelly and Gigas[9] to fit another type of correlation

$$\dot{\gamma}_{SP} = 33.1 N^{1.4}, \tag{2}$$

This equation was validated in the transitional regime for a Lightnin A315 impeller.

Much of the most important work on stirred tank hydrodynamics has been devoted to the choice of an appropriate impeller or combination of impellers to maximize mixing and mass transfer on a global scale.[11–14] Because of the difficulties of studying biological media, model fluids have often been chosen as they are cheaper and easier to use. A number of articles have been published on the detailed investigation of the effect of impeller mixing on small scale structures[15–19] but only a few papers concern non-Newtonian fluids.[20–23]

The development of optical techniques such as particle image velocimetry (PIV) enables the instantaneous velocity fields to be investigated.[24] Such local and instantaneous data can be used to estimate large-scale structures[25,26] by processing velocities but also small-scale structures with information on root mean square velocity gradients and vorticity at small scales.[19,27] The application of data processing methods such as proper orthogonal decomposition (POD) to PIV data enables mean flow, periodic flow induced by the rotation of the impeller, and turbulence to be discriminated.[15,16,28]

The intention of this article is to use experimental techniques such as two-dimensional (2-D) PIV coupled with data processing based on POD to characterize the different contributions of the flow to the shear rate and dissipation. A shear-thinning fluid is chosen to behave similarly to a fermentation broth from the rheology point of view. The determination of the spatial distribution of local shear rate (mean, organized, turbulent, and total shear rate) enables the energy dissipation and the turbulent kinetic energy (TKE)to be calculated in a vertical plane of the vessel. Shear rates measured at different places in the vessel are compared with published correlations.

Theoretical Analysis

Hydrodynamic regime

For a stirred tank, the Reynolds number is defined as follows

$$\mathrm{Re} = \frac{\rho_l N D^2}{\mu}, \tag{3}$$

with N the rotational speed of the impeller and D its diameter. ρ_l is the density of the liquid and μ its dynamic viscosity. In Newtonian fluids, the flow is considered to be fully turbulent for large values of the Reynolds number, $\mathrm{Re} > 10^4$, and laminar if $\mathrm{Re} < 10$. The transition regime between fully turbulent and laminar flow patterns is thus large. One can consider that when $\mathrm{Re} < 10$, the whole tank is in laminar regime whereas when $\mathrm{Re} > 10^4$, the whole tank is in turbulent flow. The transition regime may correspond to spatial heterogeneity of flow regime in the tank with turbulent flow close to the impeller and laminar flow far from it. It is typically the case when yield stress fluids are used (presence of cavern).

Power number, dissipation, and shear rate

Knowing the power number of the impeller, the power draw can easily be calculated from

$$P = \rho_l N_p N^3 D^5, \tag{4}$$

with N the agitation speed and D the impeller diameter. In the fully turbulent regime, the power number N_p is constant, whereas in laminar flow, it is inversely proportional to the Reynolds number.

The volume average of the dissipation rate of kinetic energy $\langle \varepsilon \rangle$ expressed in W/kg or m^2/s^3, is related to the power through

$$\langle \varepsilon \rangle = \frac{P}{\rho_l V_l}, \tag{5}$$

with V_l the volume of liquid in the tank.

In laminar flow, the local value of the dissipation rate of kinetic energy can be written as

$$\bar{\varepsilon} = \frac{2}{\rho_l} \cdot \mu \, \overline{S_{ij}} \, \overline{S_{ij}}, \tag{6}$$

where S_{ij} are the components of the mean strain rate (or stretching) tensor S

$$\overline{S_{ij}} = \frac{1}{2} \cdot \left(\frac{\partial \overline{U_i}}{\partial x_j} + \frac{\partial \overline{U_j}}{\partial x_i} \right). \tag{7}$$

This dissipation rate can be easily measured by optical techniques such as PIV. In turbulent flow, the local value of the dissipation rate of TKE can be written as

$$\bar{\varepsilon} = \frac{2}{\rho_l} \cdot \mu \, \overline{s'_{ij} s'_{ij}}, \tag{8}$$

with

$$s'_{ij} = \frac{1}{2} \cdot \left(\frac{\partial u'_i}{\partial x_j} + \frac{\partial u'_j}{\partial x_i} \right). \quad (9)$$

It is much more difficult to estimate the dissipation rate of TKE experimentally by optical techniques such as PIV, because this assumes that instantaneous and local gradients of turbulent velocity can be measured at the smallest scales of the flow.

The shear rate being a key parameter of this study, a first estimation can be proposed based on global quantities. The global shear rate $\langle \dot{\gamma} \rangle$ can be derived as

$$\langle \dot{\gamma} \rangle = \sqrt{\frac{\langle \varepsilon \rangle}{\nu}}, \quad (10)$$

where ν is the kinematic viscosity of the fluid.

In laminar flow, a useful expression of the global shear rate $\langle \dot{\gamma} \rangle$ can be derived.

$$\langle \dot{\gamma} \rangle = \sqrt{\frac{\langle \varepsilon \rangle}{\nu}} = \sqrt{\frac{P}{\nu \, \rho_l V}} = \sqrt{\frac{N_p N^3 D^5}{\nu \, \frac{\pi}{4} \, T^3}}. \quad (11)$$

In the laminar regime, the power number follows the trend

$$N_p = \frac{C}{\mathrm{Re}} = \frac{C \, \nu}{N \, D^2}. \quad (12)$$

Thus, in laminar regime, the global shear rate $\langle \dot{\gamma} \rangle$ can be expressed as

$$\langle \dot{\gamma} \rangle = \sqrt{\frac{\langle \varepsilon \rangle}{\nu}} = \sqrt{\frac{4 \, C}{27 \, \pi}} N. \quad (13)$$

This expression is formally similar to the Metzner–Otto correlation (see Eq. 1). For a Rushton turbine in laminar regime, the coefficient C is close to 60–70; thus, the coefficient of N in Eq. 13 is equal to $\sqrt{\frac{4 \, C}{27 \, \pi}} = \sqrt{3}$. In turbulent regime, it is more difficult to derive a general expression. Another difficulty of this study is related to the non-Newtonian behavior of the fluid.

Shear-thinning fluids

Biological media (e.g., filamentous fungi) generally have pronounced non-Newtonian rheological behavior. The relationship between shear rate and shear stress can be determined by a rheometer. Shear-thinning fluids are usually described by the power law model. The apparent viscosity μ_a is modelled as

$$\mu_a = K_{\mathrm{PL}} |\dot{\gamma}|^{n_{\mathrm{PL}}-1}, \quad (14)$$

with K_{PL} the consistency and n_{PL} the power law index. For shear-thinning fluids with a yield stress, which is the case for the fluid studied in this work, the Herschel–Bulkley equation better describes the apparent viscosity for low shear rates

$$\mu_a = \tau_0 \cdot |\dot{\gamma}|^{-1} + K_{\mathrm{HB}} |\dot{\gamma}|^{n_{\mathrm{HB}}-1}, \quad (15)$$

with τ_0, the yield stress of the fluid.

For shear-thinning fluids, the Reynolds number is usually calculated by replacing the viscosity in Eq. 3 by the apparent viscosity μ_a at the average shear rate. The average shear rate can be calculated from the Metzner–Otto correlation (see Eq. 1).

The Eq. 1 was established in the laminar regime but is also used in the turbulent regime and in mass transfer correlations. Other approaches have been reviewed by Herbst et al.[29] and will be discussed later in this article. Using Eqs. 14 and 1, modified generalized Reynolds number can be written as

$$\mathrm{Re} = \frac{\rho_l N^{2-n} D^2}{K \cdot k_S^{n-1}}. \quad (16)$$

Due to the fact that the apparent viscosity μ_a is estimated for the average shear rate, the definition of the Reynolds number is open to discussion.

Mean flow and flow number

Different techniques have been used to determine velocity profiles close to the impeller since the pioneering works of Dyster et al.[23] and Koutsakos and Nienow.[22] The velocity profiles have been presented in terms of nondimensional ratios of U/U_{tip}, where U_{tip} is the tip velocity of the impeller. A dimensionless discharge or flow number can be deduced from the pumping capacity of the impeller

$$Fl = \frac{Q}{N \cdot D^3}, \quad (17)$$

where Q is the pumping flow rate. For a Rushton turbine, the pumping flow rate is defined as follows

$$Q = \pi (D + s) \int_{-w/2}^{w/2} U \, dz, \quad (18)$$

where s is the distance between the impeller and the velocity measurement and w is the width of an impeller blade.

POD decomposition and organized/coherent structures

POD is a linear procedure which decomposes a series of n instantaneous velocity fields into a modal base.[30] These instantaneous velocity fields can be acquired using the 2-D PIV technique in a plane. The plane of measurement contains l lines and c columns. In each point, the two components U and W (in the x and z directions) of the velocity vector are measured. Thus, the number of instantaneous velocity components is $M = 2l \cdot c$. Each instantaneous velocity field data correspond thus to a 3-D tensor with l lines and c columns, and in each point (l,c) two components of the velocity vector (U, W). These raw data tensor can be reshaped to build a vector V with a length M. Following Sirovich,[31] one can estimate a two point correlation matrix $C(M,M)$, the components C_{ij} of which are defined as

$$C_{ij} = \frac{1}{n} \sum_{k=1}^{n} V_i^{(k)} \, V_j^{(k)}. \quad (19)$$

n represents the number of instantaneous measurement planes that are needed to estimate statistical values (n is of the order of 400–1000). Each diagonal component of the matrix C corresponds to the contribution of each component of the velocity to the total variance or kinetic energy. The trace of C is thus the total kinetic energy contained in the 2-D plane of measurement. It is possible to derive the eigenvalues λ_{I} and

eigenfunctions Φ_I of the correlation matrix C, where I is the index of each mode of this decomposition. By construction, each eigenfunction Φ_I is a vector and it has the same size than the vector V. This vector can be inversely reshaped to build a 3-D tensor with l lines and c columns, and in each point (l,c) two components of the vector V which will be noted (U_I,W_I). Thus, reshaped Φ_I looks like a velocity field in the plane of measurement but it is important to note that Φ_I is a modal basis, the eigenfunctions Φ_I having no dimension. In contrast, the eigenvalues λ_I are expressed in m^2/s^2 and quantify the contribution of each mode I to the total kinetic energy in the plane of measurement.

For a better understanding, some useful properties are recalled in the next paragraph. First, the eigenfunctions are normalized and orthogonal. If (,) represents the inner product, then

$$(\Phi_I, \Phi_J) = \delta_{IJ}. \tag{20}$$

If $a_k^{(I)}$ is the result of the projection of the *k-th* instantaneous velocity field on the *I-th* mode, then each scalar $a_k^{(I)32}$ can be derived as follows

$$a_k^{(I)} = (\Phi_I, U_k). \tag{21}$$

An important property of POD decomposition is that the coefficients a_k^I are uncorrelated. Thus, the statistical average over the n realizations of each factor gives

$$\overline{\left(a_k^{(I)} a_k^{(J)}\right)} = \lambda_I \delta_{IJ}. \tag{22}$$

This property stresses that each mode makes a specific contribution to the mean field kinetic energy independently. If the eigenvalues are put in decreasing order, the number of modes necessary to estimate a significant percentage of the total kinetic energy can be estimated. One of the main advantages of POD lies in the ability to reconstruct the k^{th} instantaneous velocity field in terms of a decomposition of M components defined as

$$U_k = \sum_{I=1}^{M} a_k^{(I)} \Phi_I. \tag{23}$$

In general, the first mode can be associated with the mean velocity field.[17] This is a classic result when the POD is carried out with the instantaneous velocity fields. Moreau and Liné[28] have shown that POD can be an efficient way to separate the periodic velocity fluctuations induced by the impeller rotation without performing conditional or phase-averaged measurements. The two following modes (second and third) were shown to reveal large-scale rotating structures.[28] Their length scale was quite similar to the periodic trailing vortex size. In addition, the second and third eigenvalues were shown to be equal, meaning that the energy of the flow represented by these modes was the same. To calculate the different contributions of the fluid motion to the shear rate, it is important to reconstruct the instantaneous velocity as a sum of three main components

$$U_k = a_k^{(1)} \Phi_1 + \sum_{I=2}^{3} a_k^{(I)} \Phi_I + \sum_{I=4}^{M} a_k^{(I)} \Phi_I, \tag{24}$$

where the first term (Mode I = 1) corresponds to the mean flow, the second term (Modes I = 2 and 3) corresponds to the coherent structures (trailing vortices), and the third term (Modes I > 3) may be attributed to turbulence.

Experimental Set-Up

Mixing tank

The tank used in this study consisted of a standard cylindrical tank equipped with four equally spaced baffles (width $B = 0.045\ m = T/10$). The cylindrical tank was made of poly(methyl methacrylate) and had a diameter $T = 0.45$ m and a liquid height $H = T = 0.45$ m. The cylindrical vessel was placed in a cubic tank filled with water to minimize optical refraction. The clearance, C, was equal to the impeller diameter. More information about the mixing tank dimensions is provided in previous papers.[17,18,33]

In this work, a Rushton turbine ($D = 0.15$, $m = T/3$, $w = 0.03$ m) was used. Three agitation speeds (150, 205, and 250 rpm) were chosen to investigate three different Reynolds numbers (100, 173, and 237) estimated from Eq. 16.

Velocity profiles measured with Carbopol will be compared to profiles measured with water ($N = 150$ rpm, Re = 56250).

For further image processing, for example, for velocity calculation, calibration of the images is absolutely necessary as the processing requires a distance measured in mm units and not in pixel units. In this work, the calibration was done with a 2-D calibration plate that contained about 225 marked positions (1 mm holes). An image of the calibration plate was recorded with a complete image focused and a small camera lens aperture. This was done to calibrate the image and correct image distortions due to projection perspective and/or camera lens errors.

PIV technique

The principle of the 2-D PIV technique is to acquire instantaneous velocity fields throughout a region illuminated by a planar laser sheet. Seeding particles are introduced into the flow and their motion is used to estimate the kinematics of the local fluid. The particles are chosen to be neutrally buoyant and to scatter the light efficiently.

The motion of particles is measured using a photographic method by recording two images of the fluid flow with a short time interval between them. Image pairs are then processed by dividing the complete image into squared interrogation areas. In each 16-pixel-wide interrogation area, the cross-correlation technique enables the most probable particle displacement to be calculated.

The PIV system used in this study consisted of a laser and an image acquisition system provided by LaVision (LaVision GmbH, Goettingen, Germany). The system included an Nd-Yag laser (Quantel, 10 Hz, 200 × 2 mJ), a synchronization system and a charge-coupled-device camera (Imager Intense, 12 bits, 1376 × 1040 px^2). The camera was equipped with a Nikon lens (Micron Nikon 60 or 105 mm). Fast Fourier transform cross-correlation was used to interrogate the two images, which were divided into interrogation areas (16 × 16 px^2).

Silver-coated, hollow, glass spheres (S-HGS-10, 10 μm) were used as seeding particles. They were provided by Dantec Dynamics (Skovlunde, Denmark). These particles have a sufficiently small relaxation time that they may be considered to follow the motion of the fluid faithfully.

Table 1. Operating Conditions and Average Values of Shear Rate, Apparent Viscosity, Dissipation Rate, and Volume Ratio of the Cavern

Fluid	N (rpm)	$\langle\dot{\gamma}\rangle$ From Eq. 1 s^{-1}	$\langle\mu_a\rangle$ Pa s	$\langle\varepsilon\rangle$ W kg^{-1} (Whole Tank)	$\langle\varepsilon\rangle$ W kg^{-1} (Cavern)	Vc/V
Carbopol	150	29	0.56	0.09	0.14	0.64
	205	40	0.45	0.24	0.31	0.76
	250	48	0.39	0.42	0.52	0.81
Water	150	29	0.001	0.09	0.09	1

From each image pair, the velocity vectors were computed with Davis7® software (LaVision GmbH, Goettingen, Germany) using multipass processing and an overlap of 50%. For all experiments, 400–1000 image pairs were recorded, and statistical convergence of the velocity was checked. A spatial resolution dx of 0.7 mm was chosen in the impeller stream and 1 mm outside. The delay between the two frames in an image pair was chosen in relation to the impeller speed.

In Table 1, the global values of shear rate, apparent viscosity, and dissipation rate for each rotational speed N are estimated. Indeed, two different dissipation rates are reported: the first one is the dissipation rate in the whole tank. However, because the fluid presents a yield stress, caverns can appear. The size of the caverns was estimated experimentally and the ratio of the volume of the cavern Vc over the volume of the tank V is reported in Table 1. The dissipation rates limited to the volume of the cavern are thus estimated. At lowest rotational speed, ($N = 150$ rpm, Re = 100), the cavern represents 64% of the volume of the tank whereas at the largest rotational speed, ($N = 250$ rpm, Re = 237), it reaches 81% of the volume. Clearly, these Reynolds numbers correspond to strong spatial heterogeneity inside the tank. The plane of measurements (6×6 cm^2) is located close to the impeller, in the region of the jet, where the intensity of the flow is maximum. In this region, the PIV velocity data will be processed to determine the mean flow, the fluctuating flow induced by the impeller rotation (organized motion), and eventually the turbulence. The existence of an inertial range of turbulence close to the impeller at such modest Reynolds numbers is open.

Non-Newtonian fluid

In the present work, Carbopol 980 (0.08%; Noveon Inc., Waterloo, ON) was chosen because of its high transparency even at high apparent viscosity. Carbopol 980 comes as a fine polymer powder. Once the polymer has been added to water, a neutralizer must be added to thicken the solution. The preparation began with a slow addition of the desired amount of Carbopol 980 to distilled water. The solution was mixed for 4–6 h until all the powder was dissolved in the liquid. Then, the agitation was stopped to allow the bubbles to escape and to completely hydrate the molecules. Then, the solution was neutralized to a pH of 6–9 with 50 mL of 5N NaOH solution injected in the middle of the vessel according to the manufacture's recommendations.

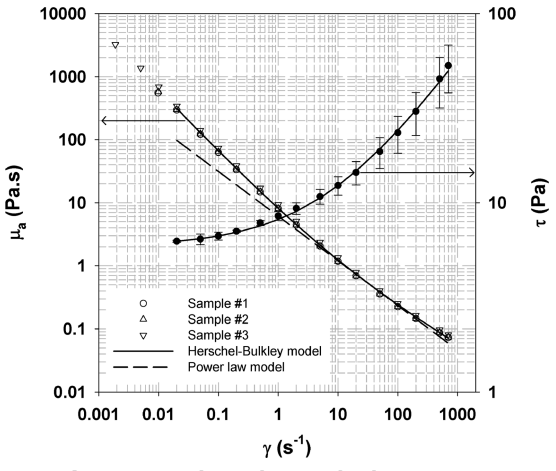

Figure 1. Apparent viscosity and shear stress versus shear rate for three samples of Carbopol 980 at 0.08%.

Rheological measurements

Rheological measurements were carried out using a Haake Mars III rheometer (Thermo Scientific, Germany) in controlled shear rate mode. A serrated plate geometry (P60/Ti L) was used to avoid wall slip effects at low-shear rate.[34,35] The temperature was fixed at 20°C. To check the stability of the liquid viscosity, three samples were taken from the tank: one at the beginning, one in the middle, and one at the end of the experiments. Rheological data were fitted to the Herschel–Bulkley equation and the power law models.

Results

Rheological properties of the fluid

Apparent viscosity and shear stress are presented vs. shear rate for three samples of the fluid in Figure 1. The fluid is non-Newtonian, shear thinning and with a yield stress. The rheological data were fitted to the power law model (Eq. 14) in the range of 10–700 s^{-1} and to the Herschel–Bulkley model (Eq. 15) for the whole range of shear rates (0.02–700 s^{-1}). Fitted parameters are presented in Table 2. Both models are compared with experimental data in Figure 1. The Herschel-Bulkley model shows better agreement for the whole range of shear rates.

Mean flow

Mean flow velocity components can be derived by a classical statistical average of the instantaneous velocity fields. Let U_k and W_k be the horizontal (radial) and vertical components of each velocity vector measured in a plane. The statistical average of the velocity is defined at each point (x,z) of the plane as

$$\overline{U}(x,z) = \frac{1}{n}\sum_{k=1}^{n} U_k(x,z), \tag{25}$$

Table 2. Rheological Parameters fitted to Eqs. 14 and 15

Fluid	τ_0 (Pa)	n_{PL} or n_{HB}	K_{PL} or K_{HB} (Pa s^n)
Power law model	–	0.29	6.12
Herschel-Bulkley model	5.9	0.45	2.29

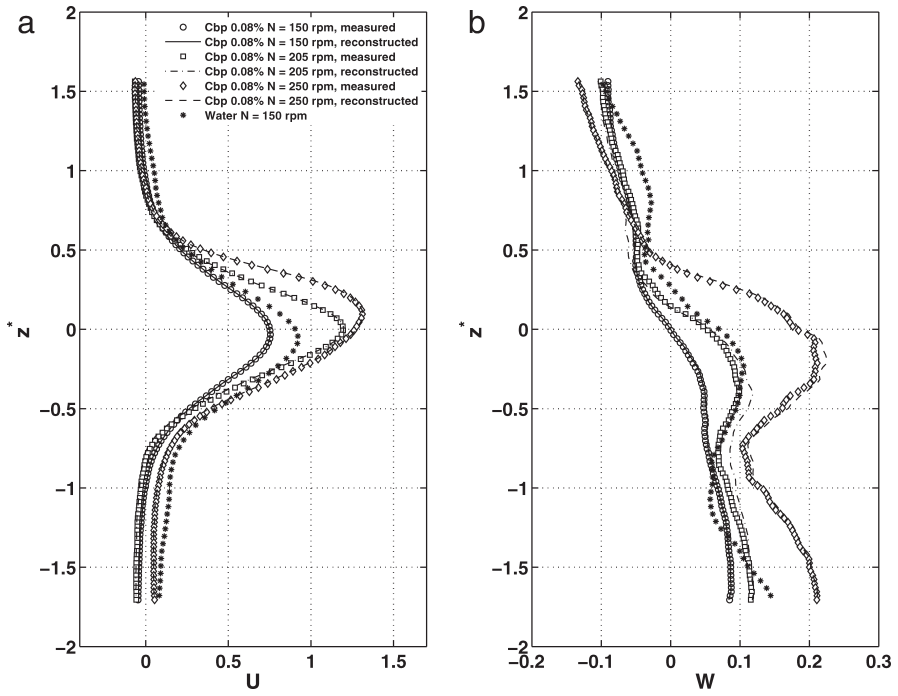

Figure 2. Radial and vertical components of mean velocity for water at 150 rpm and Carbopol 980 at 150, 205, and 250 rpm at $r/R = 1.07$: (a) radial velocities and (b) vertical velocities.

and

$$\overline{W}(x,z) = \frac{1}{n}\sum_{k=1}^{n} W_k(x,z). \tag{26}$$

In Figure 2a, the vertical profiles of the mean radial velocity for water at 150 rpm and Carbopol 980 at 150, 205, and 250 rpm are plotted vs. the normalized vertical coordinate z*=2z/w at a given radial position $r/R = 1.07$ close to the impeller. The maximum velocity obtained in water (0.9) agrees well with a previous work.[17] For the three velocities in the 0.08% Carbopol, the mean velocity profiles are relatively similar. At 150 rpm, the velocity measured in 0.08% Carbopol is lower than in water. This proves that there is an influence of the rheology on the mean flow. In Figure 2b, the vertical profiles of mean radial velocities in 0.08% Carbopol are compared to measurements in water at $r/R = 1.0$. At the impeller level, and in 0.08% Carbopol, the vertical velocity is nil for $N = 150$ rpm. This indicates that the flow is purely radial in this condition. At the same velocity, W is quite different and seems to be close to W in 0.08% Carbopol at 205 rpm. For the two higher velocities, the shape is quite similar to that of the water measurement.

The flow number quantifies the pumping capacity of an impeller. It is possible to estimate the pumping flow rate (given by Eq. 18) and to deduce the impeller flow number, Fl, (Eq. 17). In the case of water (Re = 56,250), the flow number is close to 0.7 which is a usual value for a Rushton turbine. However, for the three impeller velocities corresponding to Reynolds numbers between 100 and 250, in the transitional regime, the flow number is roughly constant (Fl = 0.5) but slightly smaller than the flow number obtained with water. This value of the impeller flow number cannot be predicted by an existing correlation obtained with non-Newtonian fluids, such as carboxy methyl cellulose (CMC) and Natrosol by Koutsakos and Nienow.[22] As discussed by Venneker et al.,[21] the flow number increases sharply with the Reynolds number in the laminar flow regime (Re < 10–100), then increases gradually in the transition regime, and finally reaches a plateau in the turbulent regime (Re > 10^4). The difference between our results and Koutsakos and Nienow's[22] data may be due to the flow index of the fluids. Considering that Fl depends strongly on high velocities, flow indices calculated with the power law model are considered. In our case, $n_{PL} = 0.29$, whereas in Koutsakos and Nienow[22] $n_{CMC} = 0.42$–0.57 and $n_{Natrosol} = 0.37$–0.56. As proposed by Venneker et al., [21] a family of curves Fl(Re) may exist, one for each value of the flow index n.

POD decomposition and reconstruction

The percentage variation of the kinetic energy associated with the M modes is plotted on Figure 3 in terms of normalized eigenvalues λ_I^* defined as

$$\lambda_I^* = \frac{\lambda_I}{\sum_{J=1}^{M} \lambda_J}. \tag{27}$$

Each symbol corresponds to a value of the impeller rotational speed N. In terms of eigenvalues, as shown in Table 3, the first mode contains 91, 80, and 69 percent of the total kinetic energy for a rotational speed corresponding to 150, 205, and 250 rpm, respectively. This first mode will be analyzed in the second part and will be shown to correspond to the mean flow. A characteristic feature of Figure 3 is that the following two modes (second and third) have roughly the same amount of kinetic energy whatever the rotational speed (see Table 3). In addition, the kinetic energy of these modes is one decade lower than that of the first mode. These Modes 2 and 3 will be analysed in the third part and shown to correspond to organized motion. Whatever the impeller rotational speed N, each of the following modes contains less kinetic energy. These modes will be discussed in the fourth part.

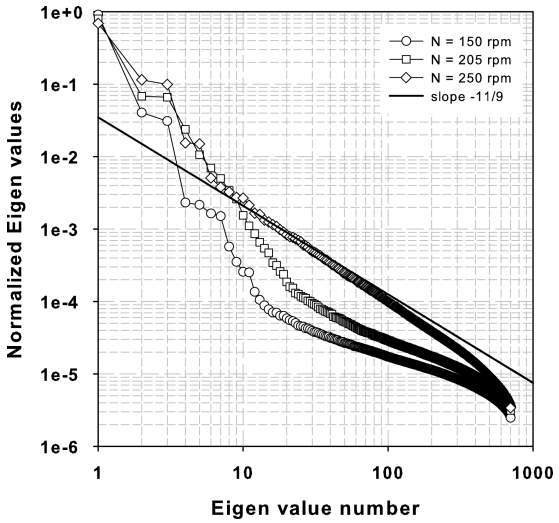

Figure 3. Evolution of the normalized eigenvalue according to the mode number.

In terms of eigenfunctions, each reshaped eigenfunction Φ_I can be plotted in the plane of measurement. As aforementioned, each reshaped Φ_I is composed of vectors whose components will be noted (U_I,W_I). Each eigenfunction Φ_I has the same size as each instantaneous velocity field (l,c). The eigenfunctions Φ_I associated with different modes I are plotted in Figure 4.

As will be discussed later, the first mode of the POD decomposition of the velocity fields is close to the mean flow (Φ_1 plotted in Figure 4a). Modes 2 and 3 (Φ_2 and Φ_3 plotted in Figures 4b, c) exhibit large rotating structures that are almost symmetric with respect to the plane of the impeller. Mode 4 (Figure 4d) looks like a flapping jet similar behavior was observed in water.[28] Modes higher than 4 are no longer symmetric and do not seem to represent any organized motion. To highlight the difference between the organized Modes 2–3 and higher modes, two Modes 11 and 12 are plotted (Φ_{11} and Φ_{12} plotted in Figures 4e and 4f) and will be related to the turbulence.

The distinction between organized motion and turbulence is a basic question in the analysis of the flow and in the understanding of mixing. To propose quantitative arguments to separate organized motions from turbulence, both eigenvalues λ_I (or $a_k^{(I)}$ coefficients) and eigenfunctions Φ_I need to be analyzed in depth. The distribution of the $a_k^{(I)}$ coefficients will be plotted for different modes I.

The $a_k^{(I)}$ coefficients are plotted in Figure 5. For the first mode, it can be seen that the distribution of $a_k^{(1)}$ is weakly dispersed around a constant value, close to 34 m/s. For the Modes 2 and 3, the distributions of the $a_k^{(2)}$($a_k^{(3)}$ not shown) coefficients associated with Modes 2 (and 3) are centered on 0 and exhibit higher percentages near the highest and lowest values of $a_k^{(2)}$. The distributions of the $a_k^{(I)}$ coefficients associated with modes higher than 4 are still centered on 0 but exhibit higher percentages for values of $a_k^{(I)}$ close to zero. Such shapes of probability density functions are discussed in a textbook on turbulence.[36] It is clear that the distributions of the $a_k^{(2)}$(and $a_k^{(3)}$) coefficients look like the probability density of a sine wave, whereas the distributions of the $a_k^{(I)}$ coefficients (I larger than 4) exhibit Gaussian shapes that are characteristic of turbulent motions.

Complementary information helpful to discriminate organized motion from turbulence lies in the Φ_I eigenfunctions: radial profiles of the two components (U_I,W_I) of different Φ_I eigenfunctions are plotted in Figure 6 to compare the contributions of Mode 1 associated with the mean flow, Modes 2 and 3 associated with the organized motion and higher modes associated with turbulence. The radial component of the first mode is roughly constant, equal to 0.02; considering the almost constant value of $a_k^{(1)}$, it corresponds to a radial velocity equal to 0.02×34 m/s $= 0.68$ m/s characteristic of the mean flow in the liquid jet induced by the impeller. The vertical component of this first mode is almost zero. The radial and vertical components of Modes 2 and 3 exhibit purely sinusoidal behaviors. A higher mode has been plotted (Mode 12). The radial and vertical components of Mode 12 present many different wavelengths, the larger ones between to 0.1 R and 0.3 R. Such orders of magnitude of wavelength may be related to Taylor macroscale induced by the Rushton turbine.

It is important to keep in mind that the amplitudes of (U_I,W_I) components of Φ_I eigenfunctions are, respectively, 0.02 and 0.01. This is due to the fact that the norm of each eigenfunction in a whole plane of measurement is equal to unity. Thus

$$\sum_{i=1}^{l}\sum_{j=1}^{c}\left[U_I(i,j)^2 + W_I(i,j)^2\right] = 1. \tag{28}$$

Consequently, the order of magnitude of each vector component is $1/\sqrt{l\,c} \approx 10^{-2}$.

Mean flow characteristics associated with Mode 1

It must be recalled here that the first eigenfunction Φ_1 (plotted in Figure 4.a) looks like a velocity field but the velocity field associated with Mode 1 is given by

$$\overline{U_k} = \overline{a_k^{(1)}}\Phi_1. \tag{29}$$

The statistical averaged value of the first series of coefficients $a_k^{(1)}$ is reported in Table 4, for the three values of the impeller rotational velocity N. The values of $a_k^{(1)}$ are given in m/s. As previously shown, the magnitude of the eigenfunction components is of the order of $1/\sqrt{l\,c} \approx 10^{-2}$. Consequently, the order of magnitude of the velocity is 0.5 m/s. It is consistent with the tip velocity magnitude (1.17, 1.62, and 1.96 m/s for $N = 150$, 205, and 250 rpm). In addition, the ratio $a_k^{(1)}/U_{tip}$ is shown to be almost constant.

Table 3. Percentage of Kinetic Energy Associated with Each Mode

	% of Kinetic Energy			Kinetic Energy (m^2/s^2)
N (rpm)	Mode 1	Modes 2+3	Modes >3	All modes
150	91	7	2	1250
205	80	13	7	3053
250	69	21	10	5798

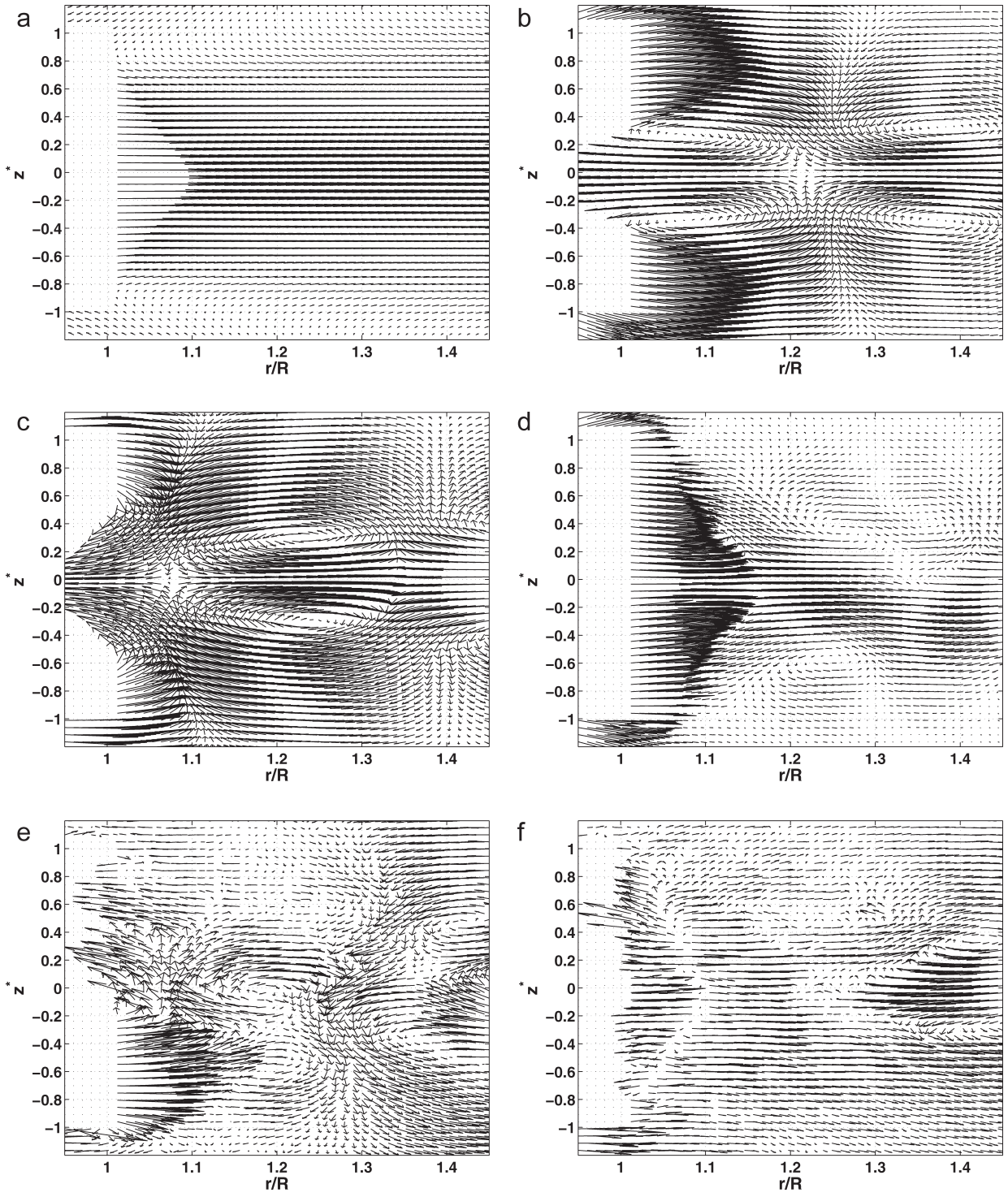

Figure 4. Plots of the modes 1, 2, 3, 4, 11, and 12 from POD: (a) Mode 1, (b) Mode 2, (c) Mode 3, (d) Mode 4, (e) Mode 11, and (f) Mode 12 for $N = 150$ rpm.

The distribution of the $a_k^{(1)}$ coefficients is plotted in Figure 5a. The mean value is 33.74; the maximum and minimum values are 31 and 37. As shown in Table 4, the standard deviations are small and represent less than 10% of the mean values. The individual values of the coefficients $a_k^{(1)}$ are thus almost equally distributed between the minimum and the maximum. Compared to the coefficients of the higher modes, $a_k^{(1)}$ coefficient can be considered as roughly constant. In addition, each value of these coefficients $a_k^{(1)}$ is close to a square root of the first eigenvalues, as expected because the coefficients $a_k^{(1)}$ show small variations around their mean value.

Recall that each realization of the velocity field may be reconstructed with a constant mean flow value plus organized and/or turbulent fluctuations. Clearly, the first mode can be associated with the mean flow. The vertical profiles of the reconstructed velocity associated with the first mode can be plotted (see Figure 2) and compared to the vertical profile of the statistical averaged value of the velocity. The radial and axial velocities reconstructed with the first mode are

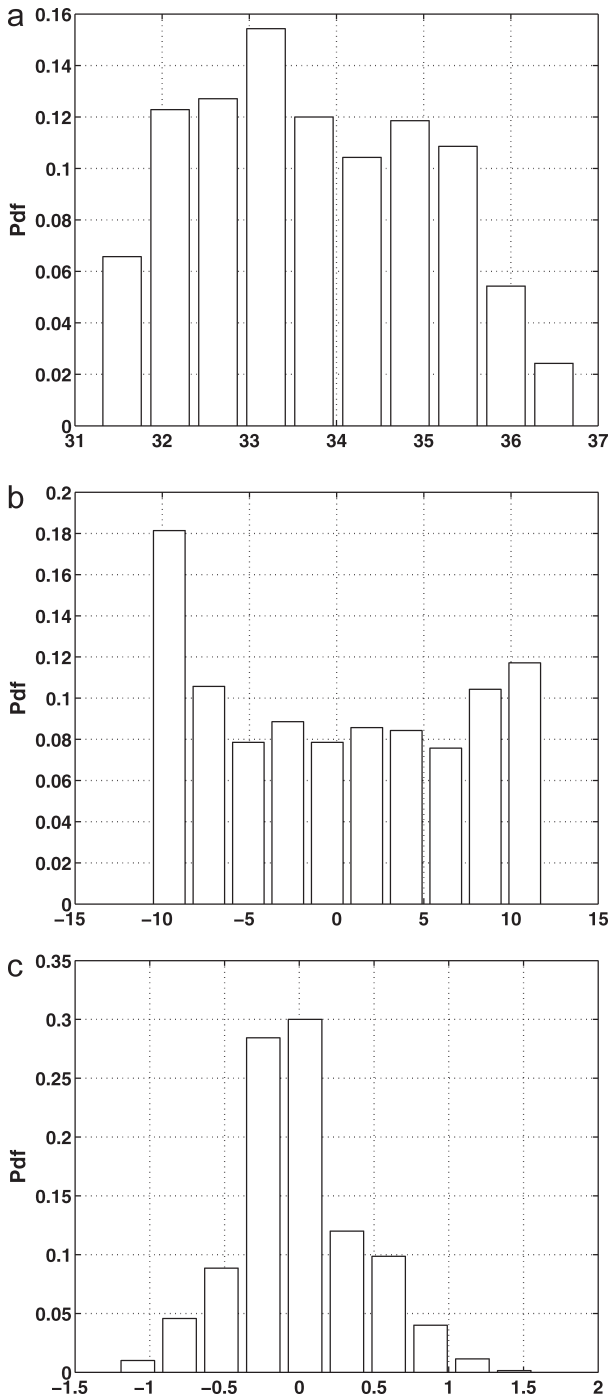

Figure 5. Distribution of the alk coefficients for modes 1, 2, 11 at N = 150 rpm: (a) Mode 1, (b) Mode 2, and (c) Mode 12.

plotted on Figure 2 in a vertical plane $r/R = 1.07$, for the three values of impeller rotational velocity. Figure 2 confirms that the first mode of the decomposition based on POD corresponds exactly to the mean flow.

The analysis of the viscous dissipation rate of kinetic energy and shear rate associated with the mean flow will be tackled in the final discussion.

Organized motion associated with Modes 2 and 3

van Oudheusden et al.[37] have shown that, when POD modes are coupled (same order), they correspond to orthogonal components of a periodic process. In our experiments (Figure 3), the second and third eigenvalues have the same magnitude whatever the rotational velocity N. However, as the 2-D PIV are not time resolved, it is not possible to plot the sinusoidal variations of scalars $a_k^{(2)}$ and $a_k^{(3)}$. Nevertheless, following van Oudheusden et al.,[37] it is possible to plot the k realizations of pairs $(a_k^{(2)}, a_k^{(3)})$ showing that this pair of eigenfunctions is orthogonal. Each series of points corresponding to $n = 700$ instantaneous values lies on a circle (see Figure 7) as

$$\frac{a_k^{(2)^2}}{2\,\lambda_2} + \frac{a_k^{(3)^2}}{2\,\lambda_3} = 1. \tag{30}$$

The radius of the each circle, given by $\sqrt{2\,\lambda_2} \approx \sqrt{2\,\lambda_3}$, increases with the impeller rotational speed N.

The periodic nature of these coherent structures associated with Modes 2 and 3 could be expressed as sinusoidal variations $a^{(2)}(\varphi_k)$ and $a^{(3)}(\varphi_k)$ as shown in previous papers[15,16]

$$a_k^{(2)} = a^{(2)}(\varphi_k) = \sqrt{2\,\lambda_2}\,\sin(\varphi_k) \tag{31}$$

and

$$a_k^{(3)} = a^{(3)}(\varphi_k) = \sqrt{2\,\lambda_3}\,\cos(\varphi_k). \tag{32}$$

Where φ_k is the phase angle. The parameters $a^{(2)}(\varphi_k)$ and $a^{(3)}(\varphi_k)$ have the dimension of velocities (m/s). It is thus possible to reconstruct the temporal evolution of the organized motion

$$U_k^{(org)} = \sum_{I=2}^{3} a_k^{(I)}\Phi_I = \sqrt{2\,\lambda_2}\,\cos(\varphi_k)\Phi_2 + \sqrt{2\,\lambda_3}\,\cos(\varphi_k)\Phi_3. \tag{33}$$

These velocity fields are plotted in Figure 8, at three instants corresponding to phase angle values (0, $\pi/4$, and $\pi/2$). The detachment of two counter-rotating organized structures is clearly highlighted, this process being periodic and induced by the blades of the impeller. The coefficients $(a_k^{(2)}, a_k^{(3)})$ are sinusoidal and orthogonal. This explains why the distribution of the $(a_k^{(2)}, a_k^{(3)})$ coefficients plotted in Figure 5 exhibits a probability density function characteristic of sine waves.

The analysis of the viscous dissipation rate of kinetic energy and shear rate associated with the organised motion will be tackled in the final discussion.

Higher order modes motion

Following the decomposition, we propose a reconstruction of the turbulence based on all the modes higher than 3.

$$U_k^{(turb)} = \sum_{I=4}^{M} a_k^{(I)}\Phi_I. \tag{34}$$

In the plane of measurement, each turbulent vector $U_k^{(turb)}$ is composed of two components (u_k', w_k'). The distributions of radial (u_k') and vertical (w_k') turbulent velocities are plotted in Figure 9 in a point located in the stream of the impeller. These distributions are Gaussian and similar to turbulent components. Referring to the central limit theorem, the Gaussian characteristic function can be expressed as

$$B(u') = \frac{1}{\sqrt{2\,\pi\,\sigma_u^2}}\,\exp\left(-\frac{u'^2}{2\,\sigma_u^2}\right). \tag{35}$$

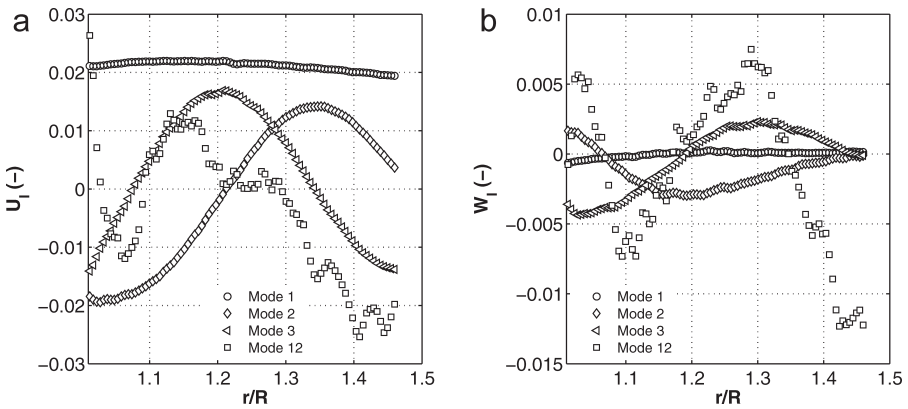

Figure 6. Comparison of radial profiles of (a) radial U_l and (b) vertical W_l components of different eigenfunctions λ_l for Modes 1, 2, 3, and 12 for $N = 150$ rpm.

The probability density functions (pdf) of radial (u_k') and vertical (w_k') turbulent velocities are plotted on Figure 9, for a point located close to the upper right corner of the impeller. The Gaussian distributions have been plotted on the same graphs, with the experimental values of the standard deviations of each velocity fluctuation ($\sigma_u = 0.024$ *m/s* and $\sigma_w = 0.022$ *m/s*). There is good agreement between the experimental and the Gaussian *pdf*s.

From these experimental values of turbulent fluctuations of the velocity, the TKE can be estimated as

$$k^{(\text{turb})} = \frac{3}{4}\left(\overline{u'^2} + \overline{w'^2}\right). \tag{36}$$

The vertical profile of the square root of the TKE normalized by the tip velocity $\sqrt{k^{(\text{turb})}}/U_{\text{tip}}$ is plotted in Figure 10a, close to the impeller at a given radial position $r/R = 1.07$. This ratio $\sqrt{k^{(\text{turb})}}/U_{\text{tip}}$ gives an order of magnitude of the turbulent intensity between 5 and 20%. Recall[17] that, in the case of water at $N = 150$ rpm, in the same tank but in fully turbulent flow, the ratio $\sqrt{k^{(\text{turb})}}/U_{\text{tip}}$ had the same shape, but the maximum values reached 40–50%. Such a trend of $\sqrt{k^{(\text{turb})}}/U_{\text{tip}}$ vs. Reynolds numbers was expected because the turbulent intensity quantifies the level of turbulence. Carbopol data correspond to a transitional flow pattern ($100 <$ Re < 250), whereas water data correspond to fully turbulent flow (Re $= 56{,}250$). Once again, the transition regime in a tank can be understood as heterogeneous flow. Close to the impeller, the flow is turbulent whereas far from it, it may be laminar.

The dissipation rate of TKE (Eq. 6) can be estimated directly from the experimental values of the instantaneous velocity. The vertical profile of the dissipation rate of TKE normalized by $N^2\ D^3$ is plotted in Figure 10b, at the same position as the profile of TKE ($r/R = 1.07$). Outside the jet of the impeller, the values of $\varepsilon^{(\text{turb})}/(N^3\ D^2)$ are similar and close to 1–2. In the region of the jet induced by the impeller, $\varepsilon^{(\text{turb})}/(N^3\ D^2)$ presents maxima that can reach 5–10. It is interesting to compare these values to a global estimation of the dissipation. It can be shown that

$$\frac{\left\langle \varepsilon^{(\text{tot})} \right\rangle}{N^3\ D^2} = \frac{4\ N_p}{27\ \pi}. \tag{37}$$

In the case of a Rushton turbine, the power number N_p is close to 5 and, thus, the global value of the normalized dissipation rate is equal to 0.23, whatever the value of the impeller velocity. The profiles of $\varepsilon^{(\text{turb})}/(N^3\ D^2)$ show that the local dissipation rate of TKE can be 5 to 20–40 times its global averaged value.

In our experiments, the velocity field was investigated in a region located close to the impeller. In Figure 3, only the eigenvalues corresponding to the highest rotational speed ($N = 250$ rpm) show a—11/9 power scaling which is a characteristic of inertial range of turbulence, as shown by Knight and Sirovich,[38] even at such a modest Reynolds number. In this case, the knowledge of local values of both TKE and its rate of dissipation enable us to estimate the characteristic

Table 4. Analysis of the First Mode Coefficients a^I_k in m/s

	First Mode Analysis (Values Are in m/s)			
N (rpm)	Mean Value $\overline{a}_k^{(1)}$ (m/s)	Square Root of the First Eigenvalue	Standard Deviation of $\overline{a}_k^{(1)}$	$\overline{a}_k^{(1)}/U_{tip}$
150	33.74	33.73	1.325	29
205	49.02	49.4	5.14	30
250	63.14	63.25	4.06	32

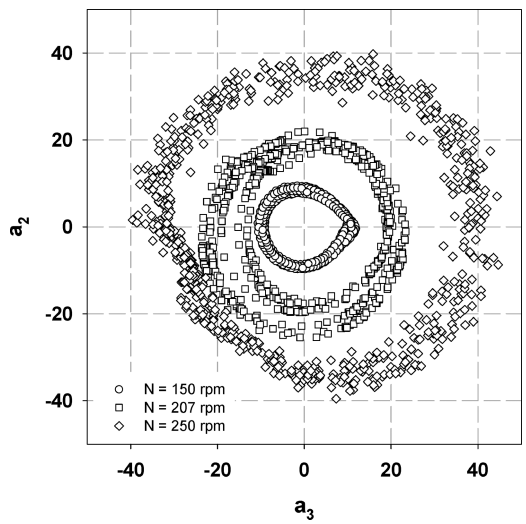

Figure 7. Distribution of pairs of coefficients ($a_k^{(2)}$, $a_k^{(3)}$) for the *n* realizations and for each impeller rotational speed *N* (150, 205, and 250 rpm).

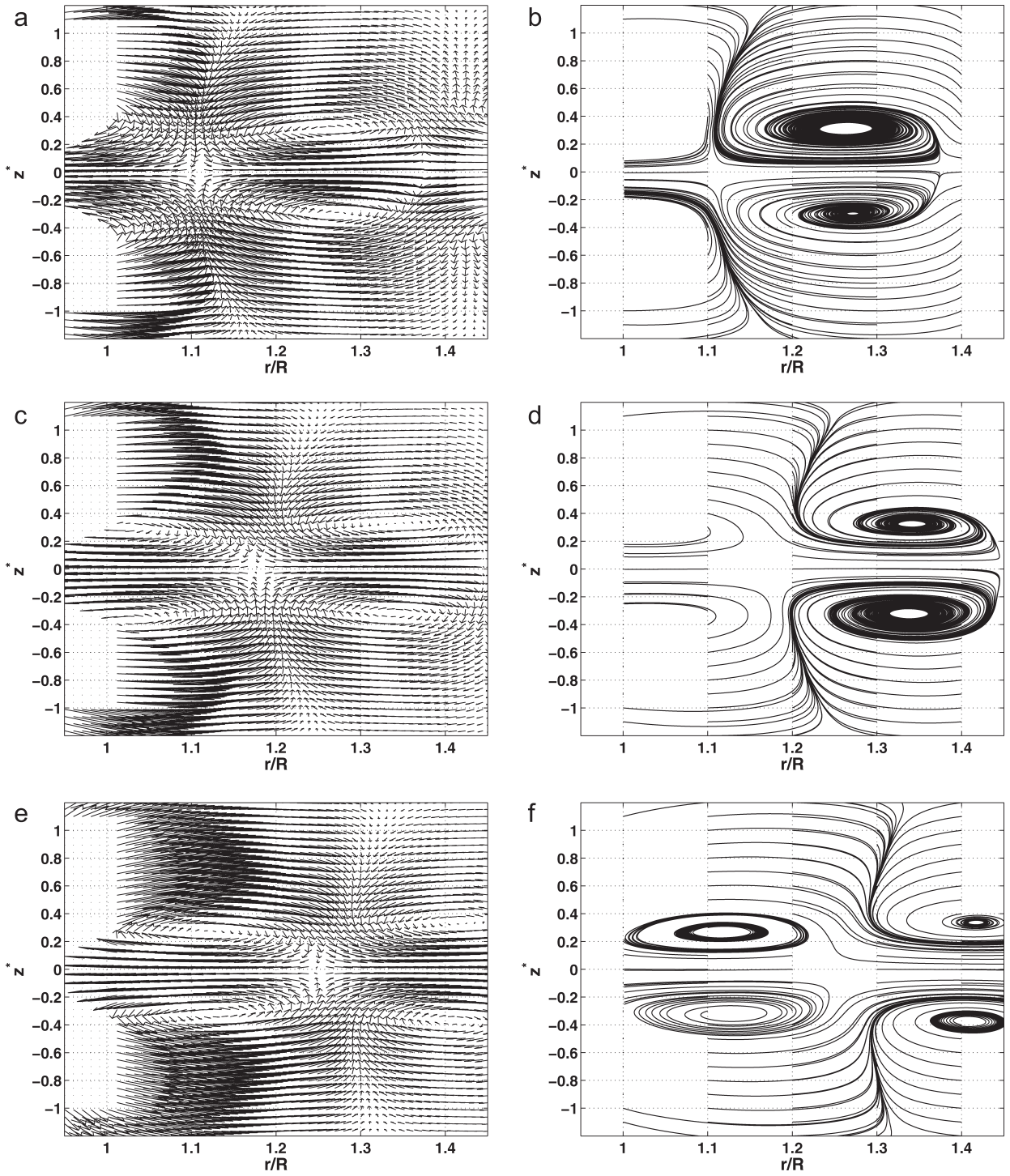

Figure 8. Plots of the velocity fields and stream function associated with the organized flow from Modes 2 and 3: (a,b) $\varphi = 0$, (c,d) $\varphi = \pi/4$, and (e,f) $\varphi = \pi/2$.

scales of the turbulence, the Taylor microscale and the Kolmogorov microscale defined as

$$\lambda_{\text{Taylor}} = \sqrt{\frac{10\ v_a\ k^{(\text{turb})}}{\varepsilon^{(turb)}}} \tag{38}$$

$$\eta_{\text{Taylor}} = \left(\frac{{v_a}^3}{\varepsilon^{(\text{turb})}}\right)^{1/4}. \tag{39}$$

These two length scales were calculated. In the jet of the impeller, the Taylor microscale varied between 2 and 4 mm, whereas the Kolmogorov microscale varied between 0.5 and 2 mm. All these scales being larger than the interrogation area of the PIV, the previous processing is validated.

Discussion

The aim of this discussion is to estimate the spatial distribution of the shear rate (the apparent viscosity can be deduced directly from the shear rate using Eq. 14 or 15). The first question is related the spatial heterogeneity of the shear rate. The second concerns the space averaged values of the shear rate and the corresponding value of the

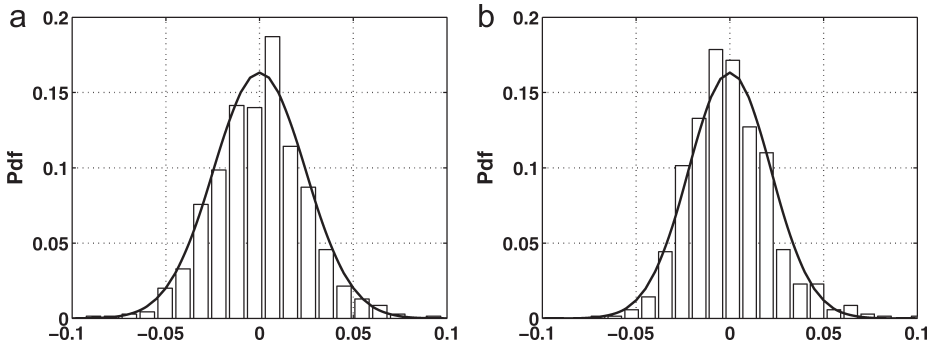

Figure 9. Radial and axial turbulent velocity distributions in the impeller stream level for $N = 150$ rpm.

Reynolds number. Up to now, the space averaged value of the shear rate has been based on the Metzner–Otto correlation[7] (see Eq. 1).

In the case of a shear-thinning fluid, the rate of viscous dissipation of kinetic energy ε is

$$\varepsilon = 2\, \nu_a\, \overline{S : S}. \tag{40}$$

This viscous dissipation rate of kinetic energy ε can be estimated at each point of the plane of measurement. Similarly, the shear rate $\dot{\gamma}$ can be estimated locally as

$$\dot{\gamma} = \sqrt{2\, \overline{S : S}}. \tag{41}$$

As only 2D PIV were performed in the study, the shear rate is estimated with the experimental measurements of $\frac{\partial U_1}{\partial x_1}$, $\frac{\partial U_1}{\partial x_2}$, $\frac{\partial U_2}{\partial x_1}$, $\frac{\partial U_2}{\partial x_2}$, the last velocity gradient $\frac{\partial U_3}{\partial x_3}$ being estimated by assuming the divergence of the velocity to be nil. The apparent viscosity μ_a can be estimated locally as a function of the local shear rate $\dot{\gamma}$. The spatial heterogeneity of both the shear rate $\dot{\gamma}$ and the apparent viscosity μ_a can be addressed. In fully turbulent flow [17], the dissipation rate of TKE is larger than the dissipation rates of organized motion and mean flow, which are negligible. It will be interesting here to estimate the respective contributions of the mean flow, organized motion and turbulence to the shear rate $\dot{\gamma}$ in transition regime.

The instantaneous strain rate (or stretching) tensor S has components S_{ij} that are defined as

$$S_{ij} = \frac{1}{2} \cdot \left(\frac{\partial U_i}{\partial x_j} + \frac{\partial U_j}{\partial x_i} \right). \tag{42}$$

Considering the POD, each instantaneous velocity vector component can be expressed in terms of the modes as

$$U_{i,k} = \sum_{I=1}^{M} a_k^{(I)} U_{I,i}. \tag{43}$$

After some derivations taking into account the fact that the coefficients a_k^I of the POD decomposition are uncorrelated (Eq. 22), we obtain

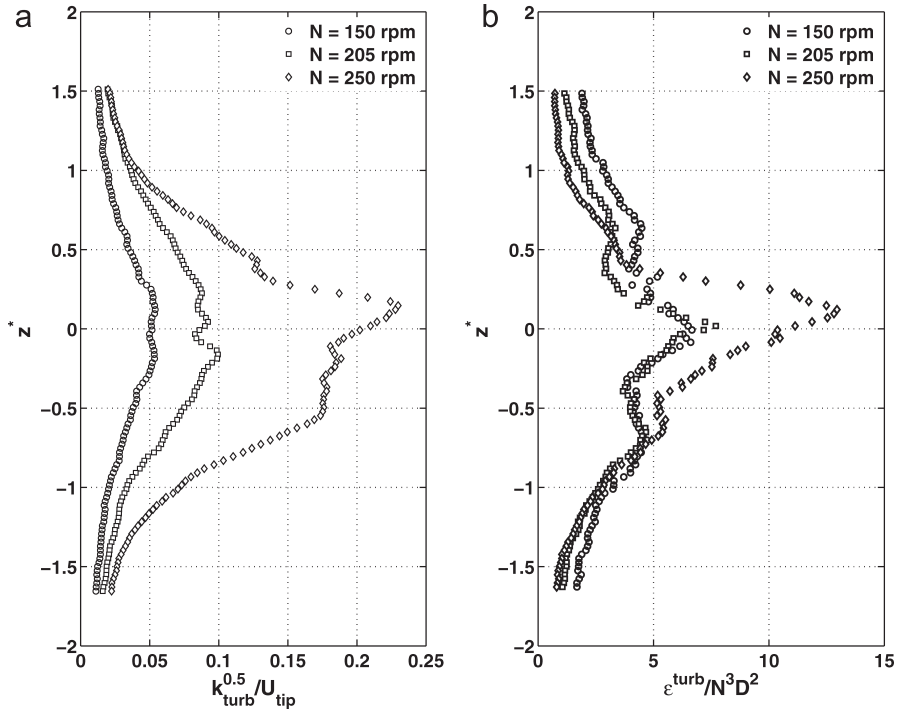

Figure 10. Profiles of normalized turbulent kinetic energy and dissipation rate in 0.08% Carbopol at three agitation speeds.

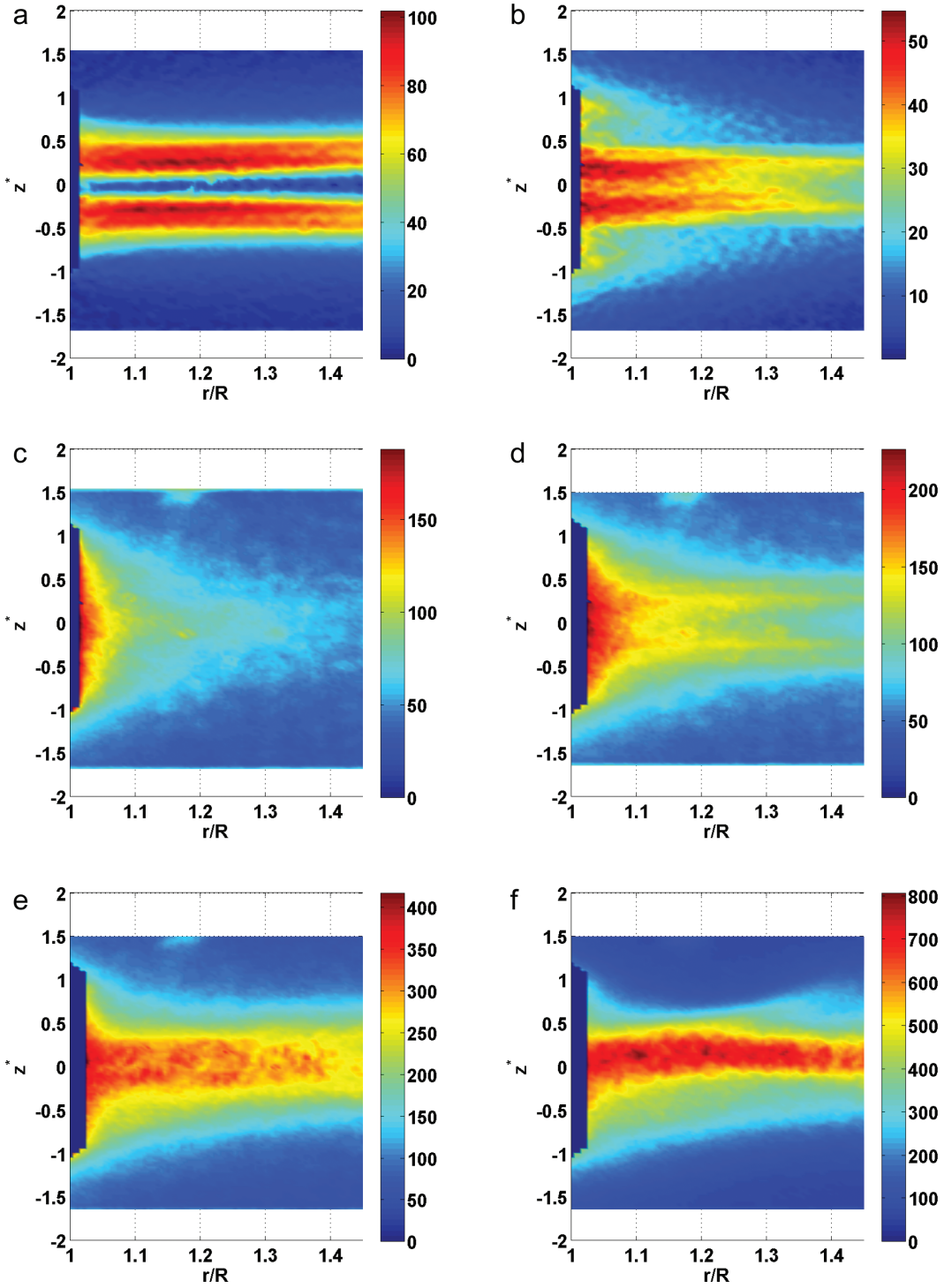

Figure 11. Local shear rate corresponding to: (a) the mean flow for N = 150 rpm, (b) the organized flow for N = 150 rpm, (c) the turbulent flow for N = 150 rpm, (d) the instantaneous flow for N = 150 rpm, (e) the instantaneous flow for N = 205 rpm, and (f) the instantaneous flow for N = 250 rpm.

$$\varepsilon = \varepsilon^{(\text{mean})} + \varepsilon^{(\text{org})} + \varepsilon^{(\text{turb})} = 2\, v_a(\dot{\gamma})\, \overline{S} : \overline{S} = 2\, v_a(\dot{\gamma}) \left[\overline{S} : \overline{S} + \overline{S^{(\text{org})} : S^{(\text{org})}} + \overline{s' : s'} \right]. \quad (44)$$

This result is very important for the rest of the analysis. Similarly, it can be shown that the shear rate $\dot{\gamma}$ can be decomposed into three parts as follows

$$\dot{\gamma} = \sqrt{\dot{\gamma}^{(\text{mean})^2} + \dot{\gamma}^{(\text{org})^2} + \dot{\gamma}^{(\text{turb})^2}}. \quad (45)$$

The local distributions of shear rate associated with mean flow, organized motion, and turbulence are plotted on Figure 11a, 11b, 11c for an rotational speed N = 150 rpm.

In terms of maximum values, the turbulent shear rate reaches 150 s^{-1}, whereas the mean flow shear rate is up to 100 s^{-1} and the organized motion shear rate is less than 50 s^{-1}. The first remark is that the shear rates (and viscous dissipation of kinetic energy) associated with the mean motion and organized motion are far from negligible compared to the turbulence. This result is significantly different from fully turbulent flow. In terms of spatial distribution, the mean flow shear rate is high in the regions of large velocity gradients along the boundaries of the liquid jet induced by the Rushton turbine. The shear rate associated with the organized motion is high close to the impeller in the region of the core of the jet; radially, it vanishes at a distance equal to R/4. The shear rate associated with turbulence is high over a large region of production of turbulence. The total shear rate is plotted on Figure 11d. It is mainly controlled by the mean flow and the turbulence. When the Reynolds number increases, Figure 11e, f, the contribution of the turbulence increases and the trace of the border of the jet decreases. The slightly upward direction of the liquid jet is also discernible on these figures.

The maximum values of the shear rate are close to 200, 400, and 800 s^{-1} for impeller velocities N of 150, 205, and 250 rpm. In fact, the shear rate is a function of the viscous dissipation rate and the apparent viscosity, which itself is a function of the shear rate. We can write

$$\dot{\gamma} = \sqrt{\frac{\varepsilon}{\nu_a}} = \sqrt{\frac{\rho\ \varepsilon}{K\ \dot{\gamma}^{n-1}}}. \tag{46}$$

Thus, it can be deduced that the shear rate is related to the viscous dissipation and to the impeller velocity as

$$\dot{\gamma}^{n+1} = \frac{\rho\ \varepsilon}{K}, \tag{47}$$

as published in previous papers.[10,39]

In turbulent flow, if the dissipation rate was proportional to $N^3\ D^2$, the shear rate $\dot{\gamma}$ would vary as $N^{\frac{3}{n+1}}$. The flow behavior index n being 0.29 with the power law model, the exponent of N would be 2.3. When the impeller velocity is multiplied by 250/150 = 1.6, the maximum shear rate is multiplied by 3.5–4, whereas $1.6^{\frac{3}{n+1}} \approx 3$. This means that the local dissipation is, not exactly but almost, proportional to N^3. This result was observed in Figure 10 where the dissipation rates of TKE seemed to be normalized by $N^3\ D^2$ in the major part of the plot, except in a restricted region (located in the impeller plane) where the ratio $\varepsilon/(N^3\ D^2)$ was twice as large for the highest impeller velocity as for the lowest one.

To conclude on the variation of the shear rate with the impeller velocity N, the histogram of shear rate was plotted (not shown) in the region of the impeller that has been extensively analyzed in this paper ($-3 < z^* < 3$ and $1 < r/R < 1.4$), but also in two vertical planes located above ($z^* > 3$), and one vertical plane located below ($z^* < -3$) the plane of measurement. In the region of the impeller ($-3 < z^* < 3$), three characteristic values of shear rate were noted: $\dot{\gamma}_{max}$ which corresponds to the maximum value of the shear rate, $\dot{\gamma}_{jet}$ which corresponds to the largest peak (most probable value in the jet of liquid), $\dot{\gamma}_{impeller}$ which corresponds to the lowest peak (most probable value outside the jet of liquid). In the three other planes ($z^* > 3$ and $z^* < -3$), $\dot{\gamma}_{far}$ corresponds to the single peak (most probable value in the three planes far from the impeller). These different

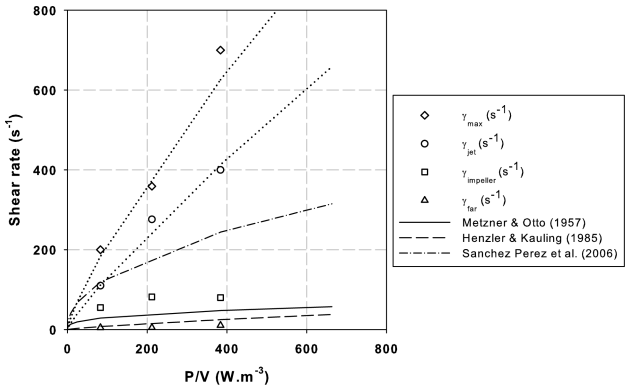

Figure 12. Evolution of the four shear rates measured in 0.08% Carbopol vs. the volumetric power dissipation in the vessel.

Data are compared to published correlations.

characteristic shear rates are plotted in Figure 12 vs. the power per unit volume as it seems to be a key parameter. $\dot{\gamma}_{max}$ and $\dot{\gamma}_{jet}$ exhibit the same trend with a power law for which the exponent is close to $1/(n+1)$. The shear rates calculated from Eqs. 1 and 47 lie between the experimental determination of $\dot{\gamma}_{impeller}$ and $\dot{\gamma}_{far}$. The correlation[10] gives a value between $\dot{\gamma}_{impeller}$ and $\dot{\gamma}_{jet}$. However, this correlation was established for an axial impeller. Thus, the constant in Eq. 2 may vary with the impeller type.

In Figure 10b, we observed that, locally, the ratio $\varepsilon/(N^3\ D^2)$ is close to 5 for the three agitation speeds in $z^* = \pm 0.5$. This local value is 20 times larger than the global value $\langle\varepsilon\rangle/(N^3\ D^2)$, which is constant and close to 0.25. With this in mind, the normalized dissipation can be approximated by

$$\frac{\varepsilon}{N^3 D^2} \approx 20\frac{\langle\varepsilon\rangle}{N^3 D^2} \approx Np, \tag{48}$$

for a standard vessel with $H/T = 1$ and $D/T = 1/3$.

In Eq. 47, ε can be replaced by $Np{\cdot}N^3D^2$. Thus, the shear rate becomes

$$\dot{\gamma} = \left(\frac{\rho\ N_p\ D^2}{K}\right)^{\frac{1}{n+1}} N^{\frac{3}{n+1}}. \tag{49}$$

It can be noted that this expression is close to correlation 24 in Ref. [10]. In our case, Eq. 49 gives a reasonable trend for $\dot{\gamma}_{jet}$ and $\dot{\gamma}_{impeller}$. In Table 5, apparent viscosities and Reynolds numbers are calculated for the new expression of the shear rate and compared to the values obtained previously with the Metzner–Otto correlation.[7]

The new shear rate, corresponding to the most probable value of the shear rate in the impeller zone, being larger than the values predicted by the Metzner–Otto correlation, the apparent viscosity is decreased and the Reynolds number increased. When the new correlation of shear rate is taken into account, the Reynolds numbers are slightly increased but remain in the transition regime between laminar and turbulent flow.

In addition, in the regions located outside the liquid jet, and in particular far from the impeller, the turbulence level is weak. The order of magnitude of the shear rate can be satisfactorily estimated by the expression derived in the introduction (Eq. 13). This result indicates that the flow regime is not uniform in the tank, with low turbulence or even laminar

Table 5. Comparison between the Shear Rate Calculated with Eq. 1 and from the Correlation Proposed in this Work

N (rpm)	$\dot{\gamma}_{MO}$ Eq. 1 (s^{-1})	$\mu_a(\dot{\gamma}_{MO})$ (Pa s)	Re	$\langle\dot{\gamma}\rangle$ Eq. 49 (s^{-1})	$\langle\mu_a\rangle$ (Pa s)	Re
150	29	0.56	100	83	0.27	212
205	40	0.45	173	174	0.16	489
250	48	0.39	237	269	0.12	814

Apparent viscosities and Reynolds numbers are calculated following both models.

regions far from the impeller. In this article, focusing on the hydrodynamics in the impeller region, we will not go deeper into the subject of the development of laminar flow in the extremities of the vessel even when the flow close to the impeller is not.

As discussed in the experimental set-up section, four interrogation areas have been investigated using PIV in a vertical plane. It is thus possible to estimate the mean shear rate in the impeller stream zone (Z_S) located between $z^* = 3$ and $z^* = -3$ as well as the mean shear rate in the total zone investigated (Z_{tot}) located between $z^* = 15$ and $z^* = -10$. Knowing the local value of shear rate, the apparent viscosity can be calculated locally according to the rheological model and then averaged in each region. In Table 6, the average values of local apparent viscosities $\langle\mu_a(\dot{\gamma})\rangle$ are compared with apparent viscosities $\mu_a(\langle\dot{\gamma}\rangle)$ calculated with average local shear rate $\langle\dot{\gamma}\rangle$ in the zone Z_S and Z_{tot}. Even if the total volume of the vessel is not entirely represented by the zones Z_S and $Z_{tot,}$ these average values may be representative of what is going on in the tank.

It can be noted that the average shear rate $\langle\dot{\gamma}\rangle$ in Z_S is closed to the shear rate calculated from Eq. 49 and $\sim$10 times larger that the shear rate $\langle\dot{\gamma}\rangle$ in Z_{tot}, average over the total volume. In Table 6, it is shown that $\langle\dot{\gamma}_{Z_S}\rangle$ can roughly be normalized by $N^{3/(1+n)}$, and $\langle\dot{\gamma}_{Ztot}\rangle$ by N. This result confirms the previous conclusion regarding the different evolution of the four characteristic shear rates in Figure 12. In the impeller stream zone (Z_S), the shear rate is directly linked to the power draw according to Eq. 49 meanwhile the average shear rate $\langle\dot{\gamma}_{Ztot}\rangle$ in the whole tank (Z_{tot}) is proportional to the rotational speed as in Eq. 1.

In the impeller stream zone (Z_S), the apparent viscosity $\langle\mu_a(\dot{\gamma})\rangle$ was calculated by averaging local values of apparent viscosities and by taking the apparent viscosity corresponding to the average value of local shear rate $\mu_a(\langle\dot{\gamma}\rangle)$. In the impeller stream zone Z_S, both ways of calculation leads to the comparable values of apparent viscosities. This proves that in this zone Z_S, the local shear rate is relatively homogeneous. In zone Z_{tot}, the two ways of calculation differ from 2 to 4. This difference can be explained by the heterogeneity of shear rates in the vessel.

There is one order of magnitude of difference between the apparent viscosities $\langle\mu_a(\dot{\gamma})\rangle$ averaged in the impeller stream zone Z_S and in the whole tank Z_{tot} ; consequently, we can wonder on the way of calculating the Reynolds number.

Conclusions

In this study, the mixing of a non-Newtonian, shear-thinning fluid (Carbopol) has been investigated in the transitional regime between laminar and turbulent flow in a stirred tank equipped with a Rushton turbine. Rheological measurements were performed to determine the rheological parameters of Carbopol, relating the apparent viscosity to the shear rate.

2-D PIV experimental analysis was performed in the impeller stream of the Rushton turbine at three agitation speeds. Statistical averaging of the instantaneous velocities enabled the mean flow to be evaluated, which was analyzed in terms of velocity profiles and flow numbers. Data were also compared to water measurements and published works.

POD was carried out to decompose the velocity into different modes corresponding to mean flow, organized flow, and turbulence. The decomposition gave eigenvalues and eigenfunctions for each mode. Eigenvalues are associated with the contribution of each mode to the total kinetic energy while eigenfunctions refer to the velocity field (even if they have no dimension). Comparison between the velocity reconstructed with Mode 1 and statistical average values shows that the first mode can be associated with the mean flow. Modes 2 and 3 are strongly coupled and exhibit large rotating structures that are generated by the blade motion. Velocities reconstructed with higher modes follow Gaussian characteristics that can be attributed to turbulence. Using modes higher than 3, it was possible to calculate the spatial distributions of TKE and turbulent dissipation rate.

Through POD, the rate of viscous dissipation of kinetic energy and the shear rate associated with the three motions of the flow were calculated. Unlike in the fully turbulent regime, the organized and mean flows cannot be neglected in the calculation of the total viscous dissipation rate of kinetic energy in transitional regime. The local shear rate was determined in the whole tank. At each impeller velocity, four shear rates were estimated from experiments, a maximum value and three characteristic values: in the jet, outside the jet in the impeller region, and far from the impeller. These values were compared to existing correlations and a new expression proposed based on physical analysis.

This work highlights the difficulty of estimating averaged shear rate in a stirred tank. The heterogeneity of shear rate measured in the whole tank may explain the number of models found in the literature for the estimation of an averaged shear rate. Even if the shear rate is measured accurately,

Table 6. Comparisons between Apparent Viscosities Calculated for the Average Shear Rate and Average Local Apparent Viscosities

	Z_s		Z_{tot}		Z_s	Z_{tot}		
N (rpm)	$\mu_a(\langle\dot{\gamma}_{Z_s}\rangle)$	$\langle\mu_a(\dot{\gamma}_{Z_s})\rangle$	$\mu_a(\langle\dot{\gamma}_{Ztot}\rangle)$	$\langle\mu_a(\dot{\gamma}_{Ztot})\rangle$	$\langle\dot{\gamma}_{Z_S}\rangle$	$\langle\dot{\gamma}_{Ztot}\rangle$	$\frac{\langle\dot{\gamma}_{Z_S}\rangle}{N^{3/(1+n)}}$	$\frac{\langle\dot{\gamma}_{Ztot}\rangle}{N}$
150	0.27	0.29	0.88	2.7	85.5	15.7	10.1	6.3
205	0.18	0.20	0.69	2.6	159	21.5	9.1	6.3
250	0.13	0.17	0.56	2.25	270	29	9.75	6.9

there is still a long way to go to understand which shear rate really plays a role in the shear sensitivity of microorganisms or for mass transfer prediction. For future works, other impellers should be tested at the same volumetric power draw to compare shear rate ranges. The question of flow pattern in a mixing tank remains "puzzling," particularly when the flow is heterogeneous. It is the case in our experiments, where the use of a yield stress fluid (Carbopol) induces caverns: outside the cavern there is no flow but inside the cavern the flow may be turbulent close to the impeller and laminar far from the impeller.

This work also furnishes quantitative data that can be used to validate CFD studies at the same level. Once validated, CFD codes could be used to simulate higher scales. This may help to understand the influence of the shear rate on the scale-up design.

Acknowledgments

This work was supported by the French Environment and Energy Management Agency (ADEME) and IFP Energies Nouvelles.

Literature Cited

1. Gabelle JC, Jourdier E, Licht RB, Ben Chaabane F, Henaut I, Morchain J, Augier F. Impact of rheology on the mass transfer coefficient during the growth phase of Trichoderma reesei in stirred bioreactors. *Chem Eng Sci*. 2012;75:408–417.
2. Ahamed A, Vermette P. Effect of mechanical agitation on the production of cellulases by Trichoderma reesei RUT-C30 in a draft-tube airlift bioreactor, *Biochem Eng J*. 2010;49:379–387.
3. Amanullah A, Blair R, Nienow AW, Thomas CR. Effects of agitation intensity on mycelial morphology and protein production in chemostat cultures of recombinant Aspergillus oryzae. *Biotech Bioeng*. 1999;62:434–446.
4. Justen P, Paul GC, Nienow AW, Thomas CR. Dependence of mycelial morphology on impeller type and agitation intensity. *Biotech Bioeng*. 1996;52:672–684.
5. Smith JJ, Lilly MD, Fox RI. The effect of agitation on the morphology and penicillin production of penicillium-chrysogenum. *Biotech Bioeng*. 1990;35:1011–1023.
6. Patel N, Choy V, Malouf P, Thibault J. Growth of Trichoderma reesei RUT C-30 in stirred tank and reciprocating plate bioreactors. *Process Biochem*. 2009;44:1164–1171.
7. Metzner AB, Otto RE. Agitation of non-Newtonian fluids. *AIChE J*. 1957;3:3.
8. Calderbank PH, Moo-Young M. The prediction of power consumption in the agitation of non-Newtonian fluids. *Trans Inst Chem Eng*. 1959;37:26–32.
9. Kelly W, Gigas B. Using CFD to predict the behavior of power law fluids near axial-flow impellers operating in the transitional flow regime. *Chem Eng Sci*. 2003;58:2141–2152.
10. Sanchez Perez JA, Rodriguez Porcel EM, Casas Lopez JL, Fernandez Sevilla JM, Chisti Y. Shear rate in stirred tank and bubble column bioreactors. *Chem Eng J*. 2006;124:1–5.
11. Albaek MO, Gernaey KV, Stocks SM. Gassed and ungassed power draw in a pilot scale 550 litre fermentor retrofitted with up-pumping hydrofoil B2 impellers in media of different viscosity and with very high power draw. *Chem Eng Sci*. 2008;63:5813–5820.
12. Nienow AW. Gas dispersion performance in fermenter operation. *Chem Eng Progress* 1990;86:61–71.
13. Gabelle JC, Augier F, Carvalho A, Rousset R, Morchain J. Effect of tank size on kLa and mixing time in aerated stirred reactors with non-Newtonian fluids. *Can J Chem Eng*. 2011;89:1139–1153.
14. Pedersen AG, Bundgaardnielsen M, Nielsen J, and Villadsen J. Characterization of mixing in stirred tank bioreactors equipped with rushton turbines. *Biotech Bioeng* 1994;44:1013–1017.
15. Ducci A, Doulgerakis Z, Yianneskis M. Decomposition of flow structures in stirred reactors and implications for mixing enhancement. *Ind Eng Chem Res*. 2007;47:3664–3676.
16. Doulgerakis Z, Yianneskis M, Ducci A. On the Manifestation and nature of macroinstabilities in stirred vessels. *AIChE J*. 2011;57:2941–2954.
17. Escudié R, Liné A. Experimental analysis of hydrodynamics in a radially agitated tank. *AIChE J*. 2003;49:585–603.
18. Escudié R, Liné A. Analysis of turbulence anisotropy in a mixing tank. *Chem Eng Sci*. 2006;61:2771–2779.
19. Gabriele A, Nienow AW, Simmons MJH. Use of angle resolved PIV to estimate local specific energy dissipation rates for up- and down-pumping pitched blade agitators in a stirred tank. *Chem Eng Sci*. 2009;64:126–143.
20. Arratia PE, Kukura J, Lacombe J, Muzzio FJ. Mixing of shear-thinning fluids with yield stress in stirred tanks. *AIChE J*. 2006;52:2310–2322.
21. Venneker BCH, Derksen JJ, Van den Akker HEA. Turbulent flow of shear-thinning liquids in stirred tanks—The effects of Reynolds number and flow index. *Chem Eng Res Des*. 2010;88:827–843.
22. Koutsakos E, Nienow AW. *Effects of rheological properties of simulated fermentation broths on flows in stirred bioreactors: a Laser Anemometry study*. In: Carter, RE, editor. New York: Elsevier Applied Science, *Rheology of Food, Pharmaceutical and Biological Materials with General Rheology*, 1990; 284–302.
23. Dyster KN, Koutsakos E, Jaworski Z, Nienow AW. An Lda study of the radial discharge velocities generated by a rushton turbine Newtonian fluids. *Chem Eng Res Des* 1993;71:11–23.
24. Adrian RJ. Twenty years of particle image velocimetry. *Exp Fluids* 2005;39:159–169.
25. Bakker A, Myers KJ, Ward RW and Lee CK. The laminar and turbulent flow pattern of a pitched blade turbine. *Trans Inst Chem Eng*. 1996;74:485–491.
26. Sheng J, Meng H, Fox RO. A large eddy PIV method for turbulence dissipation rate estimation. *Chem Eng Sci*. 2000;55:4423–4434.
27. Delafosse A, Collignon ML, Crine M, Toye D. Estimation of the turbulent kinetic energy dissipation rate from 2D-PIV measurements in a vessel stirred by an axial Mixel TTP impeller. *Chem Eng Sci*. 2011;66:1728–1737.
28. Moreau J, Liné A. Proper orthogonal decomposition for the study of hydrodynamics in a mixing tank. *AIChE J*. 2006;52:2651–2655.
29. Herbst H, Schumpe A, Deckwer WD. Xanthan production in stirred tank fermenters: oxygen transfer and scale-up. *Chem Eng Technol*. 1992;15:425–434.
30. Lumley JL. *The structure of inhomogeneous turbulence*. In: Iaglom AM, Tatarski VI, editors. New York: Elsevier Applied Science, *Atmospheric Turbulence and Wave Propagation*, 1967; 166–178.
31. Sirovich L. Turbulence and the dynamics of coherent structures. I - Coherent structures. II - Symmetries and transformations. III - Dynamics and scaling. *Quar Appl Math*. 1987;45:561–571.
32. Patte-Rouland B, Lalizel G, Moreau J, Rouland E. Flow analysis of an annular jet by particle image velocimetry and proper orthogonal decomposition. *Meas Sci Technol*. 2001;12:1404–1412.
33. Escudié R, Bouyer D, Liné A. Characterization of trailing vortices generated by a Rushton turbine. *AIChE J*. 2004;50:75–86.
34. Magnin A, Piau JM. Cone-and-plate rheometry of yield stress fluids. Study of an aqueous gel, *J Non-Newtonian Fluid Mech*. 1990;36:85–108.
35. Roberts GP, Barnes HA. New measurements of the flow-curves for Carbopol dispersions without slip artefacts. *Rheol Acta* 2001;40:499–503.
36. Tennekes H, Lumley JL. *A First Course in Turbulence*. Cambridge: MIT Press, 1972.
37. van Oudheusden BW, Scarano F, Hinsberg NP van, Watt DW. Phase-resolved characterization of vortex shedding in the near wake of a square-section cylinder at incidence. *Exp Fluids* 2005;39:86–98.
38. Knight B, Sirovich L. Kolmogorov inertial range for inhomogeneous turbulent flows. *Phys Rev Lett*. 1990;65:1356–1359.
39. Henlzer HJ, Kauling J. *Scale-up of Mass Transfer in Highly Viscous Liquids*. Wurzburg, Germany: Wiley, 1985.

Manuscript received July 10, 2012, revision received Sept. 14, 2012, and final revision received Nov. 12, 2012.